Thermodynamic and mechanism study of syngas production via integration of nitrous oxide decomposition and methane partial oxidation in the presence of 10%NiO–La$_{0.3}$Sr$_{0.7}$Co$_{0.7}$Fe$_{0.3}$O$_{3-\delta}$

C. Khajonvittayakul[1] · V. Tongnan[1] · T. Kangsadan[1] · N. Laosiripojana[2] ·
S. Jindasuwan[3] · U. W. Hartley[1,2]

Abstract

10%NiO–La$_{0.3}$Sr$_{0.7}$Co$_{0.7}$Fe$_{0.3}$O$_{3-\delta}$ (10%NiO-LSCF3773) was synthesized using the EDTAcitrate complexing method. Non-catalytic and catalytic nitrous oxide decomposition and methane partial oxidation using 10%NiO–LSCF3773 was experimentally studied, assuming that the reactions occurred separately in a membrane reactor at feed side and permeate side. The experimental results are in good agreement with the chemical equilibrium composition calculated using Aspen Plus, and the changes of standard Gibbs free energy of each relevant elementary reactions. The mechanism of the reactions was proposed to follow Eley–Rideal surface reaction. The optimal temperature was 800 °C, under atmospheric pressure, where (1) NO$_2$ formation was not detected (2) no production of C$_2$+ and C$_3$+ (3) complete conversion of N$_2$O, CH$_4$ and O$_2$ were achieved (4) high purity syngas was obtained with no significant amount of undesired products and (5) readily utilizable syngas at the ratio of two was achieved.

Keywords Nitrous oxide decomposition · Partial oxidation of methane · Chemical equilibrium · Aspen plus · NiO-doped LSCF

✉ U. W. Hartley
  Unalome.w.cpe@tggs-bangkok.org

[1] Department of Chemical and Process Engineering, The Sirindhorn International Thai-German Graduate School of Engineering (TGGS), King Mongkut's University of Technology North Bangkok, Bangkok (KMUTNB), 1518 Pracharaj 1 Rd., Wongsawang, Bangsue, Bangkok 10800, Thailand

[2] The Joint Graduate School of Energy and Environment, King Mongkut's University of Technology Thonburi (KMUTT), 126 Prachauthit Rd., Bangrnod, Thungkru, Bangkok 10140, Thailand

[3] Department of Industrial Chemistry, King Mongkut's University of Technology North Bangkok, Bangkok (KMUTNB), 1518 Pracharaj 1 Rd., Wongsawang, Bangsue, Bangkok 10800, Thailand

Introduction

Nitrous oxide (N_2O) is one of the greenhouse gases that causes global warming. It has 300 times of the heat-trapping ability in the atmosphere more than carbon dioxide (CO_2) compared to the same amount within 100 years [1–3]. N_2O comes from both man-made and natural sources. Examples of the former are petrochemical industries (adipic acid, nitric acid plant, agriculture (use of nitrogen fertilizer), combustion processes of fossil fuels and biomass; while the latter's are volcano emission and animal wastes. [1, 4–7]. The current industrial nitrous oxide abatement in Thailand is nitrous oxide decomposition [8]. The nitrous oxide is converted to nitrogen (N_2) and oxygen (O_2) at 600–800 °C, where the non-toxic gaseous product could be released to the environment. A part from being environmentally friendly, this method is costly because it requires a lot of external energy and does not give any valuable products.

Nitrous oxide can be utilized as oxygenated feedstock in chemical and energy production (i.e. fuel cells, production of syngas, carbonyl compounds, methanol, dimethyl ether, formaldehyde and so on) [9–13]. This work focuses on syngas production, as it is not only an energy source but also an importance feedstock in which it further conversion can give other valuable chemicals such as synthetic fuel, methanol, dimethyl ether, acetic acid etc. [9–14]. The nitrous oxide will be used as an oxidant providing a synergy of N_2O utilization and syngas production simultaneously. Transition metals (Co, Fe, and Ni) [15–20], precious metals (Pd, Pt, Re, Rh) [11–13], and metal oxide compound alumina (Al_2O_3), lanthanum cobaltite ($LaCoO_3$), lanthanum cobalt iron oxide ($LaCoFeO_3$), lanthanum ferrite ($LaFeO_3$), lanthanum manganite ($LaMnO_3$), ruthenium oxide (RuO_2), yttria-stabilized zirconia (YSZ) [15, 16, 18, 21–27].

The methane partial oxidation by nitrous oxide was studied widely in a packed-bed reactor [11]. Since both methane partial oxidation and nitrous oxide decomposition are exothermic reaction, therefore, a large amount of heat could be created causing temperature runaway. The conventional packed-bed reactor also requires a separation unit leading to a high investment cost. Membrane reactors have attracted significant attention due to its ability to function as a reactor and separator at the same time. However, the methane partial oxidation using nitrous oxide has not yet been researched in a membrane reactor. The membrane reactor could eliminate the complexity of the separation process and to ease complication of the reaction, narrow down the product distribution, increase selectivity, reduce energy consumption [12, 28–33]. This work studied methane partial oxidation and nitrous oxide decomposition which supposed to occur at the feed side and permeate side of the membrane reactor, respectively. Thermodynamics is useful for process assessment and optimal condition prediction, thus in this work, chemical equilibrium of the reactions were estimated using Aspen Plus program. The reactions were experimented using $10\%NiO–La_{0.3}Sr_{0.7}Co_{0.7}Fe_{0.3}O_{3-\delta}$ ($10\%NiO–LSCF$) to investigate actual reactions and their surface mechanisms. Ni and LSCF3773 was chosen according to its economically acceptable yield and its oxygen storage capacity, respectively [34–37].

Methodology

Possible reactions

The possible reactions in the membrane reactor are tabulated in Table 1. Table 2 represents relevant mathematical formulas for the changes of the standard Gibbs free energy calculation.

At the feed side, nitrous oxide was decomposed on the surface of the membrane giving gaseous oxygen and nitrogen (1). Nitrous oxide could react with oxygen giving nitrogen dioxide as the undesired product (2). Oxygen was assumed to flow through the membrane to the permeable side and partially oxidize methane giving synthesis gas (4) and other by-products via associated reactions (5–11) [38–40]. The chemical equilibrium properties were calculated using Aspen Plus program. Changes of the standard Gibbs free energy were calculated based on heat capacity of each reactions [41, 42] using mathematical formulas presented in Fig. 5, where i denotes species of substance, γ_i is the stoichiometric coefficient of species i, ΔC_p is heat capacity. $\Delta_r H$, $\Delta_r S$, and $\Delta_r G$ are the different of enthalpy, entropy, and Gibbs free energy of reaction, respectively. T is temperature. A, B, C, D, and E are characteristic constants [43–45].

Catalyst preparation and characterization

The aqueous solution of lanthanum (III) nitrate hexahydrate ($La(NO_3)_3 \cdot H_2O$), strontium nitrate ($Sr(NO_3)_2$), cobalt Nitrate ($Co(NO_3)_2 \cdot 6H_2O$), and iron(III) nitrate ($Fe(NO_3)_3 \cdot 9H_2O$) were added stoichiometrically and stirred until

Table 1 The possible reactions in a membrane reactor

Reaction	No. of reaction
Feed side	
$N_2O \rightleftharpoons N_2 + \frac{1}{2}O_2$	(1)
$N_2O + \frac{3}{2}O_2 \rightleftharpoons 2NO_2$	(2)
Membrane	
$ABO_{3-\delta,(s)} + \frac{\delta}{2}O_2 \rightleftharpoons ABO_{3,(s)}$	(3)
Permeate side	
$CH_4 + \frac{1}{2}O_2 \rightleftharpoons 2H_2 + CO$	(4)
$C_2H_6 + O_2 \rightleftharpoons 3H_2 + 2CO$	(5)
$C_3H_8 + \frac{3}{2}O_2 \rightleftharpoons 4H_2 + 3CO$	(6)
$C_2H_4 + O_2 \rightleftharpoons 2H_2 + 2CO$	(7)
$C_3H_6 + \frac{3}{2}O_2 \rightleftharpoons 3H_2 + 3CO$	(8)
$CH_4 + \rightleftharpoons C_{(s)} + 2H_2$	(9)
$CO + \frac{1}{2}O_2 \rightleftharpoons CO_2$	(10)
$H_2 + \frac{1}{2}O_2 \rightleftharpoons H_2O$	(11)

Non-subscripted compound are in gas phase

Table 2 Equations for calculation of the changes of the standard Gibbs free energy

Equation	No.
$Cp^o = A + BT + CT^2 + DT^3 + ET^4$	(12)
$\Delta_r H^o = \Delta_r H_0^o + \int_{T_0}^{T} \Delta Cp^o dT$	(13)
$\Delta_r H^o = \Delta_r H_0^o + \left[\begin{array}{l} \Delta A(T - T_0) + \frac{\Delta B}{2}(T^2 - T_0^2) + \frac{\Delta C}{3}(T^3 - T_0^3) \\ + \frac{\Delta D}{4}(T^4 - T_0^4) + \frac{\Delta E}{5}(T^5 - T_0^5) \end{array} \right]$	(14)
$\Delta_r S^o = \Delta_r S_0^o + \int_{T_0}^{T} \frac{\Delta Cp^o}{T} dT$	(15)
$\Delta_r S^o = \Delta_r S_0^o + \left[\begin{array}{l} \Delta A \cdot In\left(\frac{T}{T_0}\right) + \Delta B(T - T_0) + \frac{\Delta C}{2}(T^2 - T_0^2) \\ + \frac{\Delta D}{3}(T^3 - T_0^3) + \frac{\Delta E}{4}(T^4 - T_0^4) \end{array} \right]$	(16)
$\Delta_r S_0^o = \frac{\Delta_r H_0^o - \Delta_r G_0^o}{T_0}$	(17)
$\Delta Cp^o = \sum_i \gamma_i (Cp^o)_i$	(18)
$\Delta_r H_0^o = \sum_i \gamma_i \left(\Delta_f H_0^o\right)_i$	(19)
$\Delta_r G_0^o = \sum_i \gamma_i \left(\Delta_f G_0^o\right)_i$	(20)
$\Delta_r G_0^o = \Delta_r H^o - T \times \Delta_r S^o$	(21)

homogeneous. EDTA-NH$_4$OH, citric acid and ethylene glycol was added dropwise while stirred continuously. The pH of the solution was kept at 6 to 7 using NH$_4$OH. The resulting solution was evaporated at 80–90 °C. The residual muddy dark red gel was left in an oven overnight at 200 °C. The sample was calcined in moving air at 1100 °C for 12 h. giving LSCF3773 powder. The powder was mixed into Ni(NO$_3$)$_2$·6H$_2$O solution. The same procedure of drying, evaporation and calcination were applied. The crystallinity of the catalysts were characterized using X-ray diffraction technique (XRD, Rigaku TTRAX III using Cu K$_\alpha$ radiation, $\lambda = 1.5418$ Å in a range of $30° < 2\theta < 80°$ with a scanning step of 0.01°). The reducibility of the catalyst was studied by H$_2$-TPR technique (H$_2$ temperature-programmed reduction). Interaction between CH$_4$ and catalyst surface was investigated by CH$_4$-TPSR technique (CH$_4$ temperature-programmed surface reaction). The catalysts was packed in a lab-scaled tubular reactor. 100 ml/min of 5%H$_2$/Ar (for H$_2$-TPR) or 5%CH$_4$/Ar (for CH$_4$-TPSR) was introduced into the system while temperature was increased at 5 °C/min from 25 to 950 °C. The consumption of the reactant and the formation of the product gases were measured by real-time quadrupole mass spectrometer gas analyzer, based on molecular weights for gases CH$_4$ (16), CO$_2$ (44), CO (28), H$_2$ (2), and Ar (40).

Experimental set-up

The schematic diagram of the rig was presented in Fig. 1. 2 g of 10%NiO–LSCF3773 was packed into a quartz tubular reactor with an inside diameter of 10 mm. The reactor was placed in the middle of an electrical furnace (Chavachote, Thailand) with 30 cm heating zone. The catalyst was reduced in 40%H_2 in Ar at 500 °C for 2 h before the reaction for all experiments. For nitrous oxide decomposition, total flow rate of 100 ml/min of N_2O (99.95%, company) balanced in Ar (99.995%, BIG) at 1:1 ratio was fed into the system using mass flow controllers (Brooks instrument flow, 0–220 ml/min). A mixture of 50 ml/min of CH_4 (40%CH_4/Ar, company), 25 ml/min of O_2 (40%O_2/Ar, company), and 25 ml/min of Ar was introduced into the reactor for methane partial oxidation at 2:1 molar ratio of CH_4 to O_2. All the experiments were isothermally operated under atmospheric pressure at temperature range of 500–1000 °C using type K thermocouple and PID temperature controller. Gas compositions were analyzed using gas chromatography method (Shimadzu GC-2014ATP).

Conversions percentages were estimated using the following equations;

$$X_i = \left(\frac{n_{i,in} - n_{i,out}}{n_{i,in}} \right) \times 100\% \tag{22}$$

Here i denotes to N_2O, CH_4, and O_2 and n_i is mole or mole flow rate of species i.
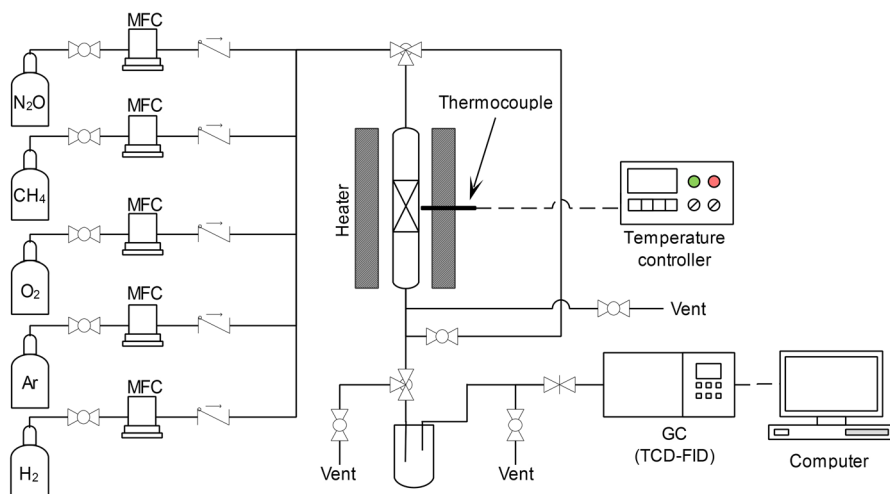
Fig. 1 Rig's diagram for nitrous oxide decomposition and methane partial oxidation

Result and discussion

Characterization techniques

X-ray diffraction

Fig. 2 shows diffractograms of (a) NiO, (b) LSCF3773, and (c) 10%NiO–LSCF3773. The XRD pattern of 10%NiO–LSCF3773 has perovskite structure and NiO as major and minor crystalline phase, respectively. The Ni-based LSCF catalyst shown the mixed XRD diffraction peaks at $2\theta = 23.20, 33.04, 37.32, 40.74, 43.36, 47.42, 53.94, 58.96, 62.92, 69.22, 75.46, 78.84$ and 80.16, the diffractograms also confirmed the presence of NiO (ICDD card No.03-065-5745; 37.32, 43.36, 62.92, 75.46, and 80.16 corresponding to (111), (200), (220), (311), and (222) planes) with a cubic crystal structure. However, there was no peak shift in XRD pattern when more doped Ni content on LSCF, which noticed that the introduction of Ni loading did not alter the crystal structure of prepared-catalyst.

H$_2$ Temperature-programmed reduction (H$_2$-TPR)

Reduction property of the synthesized NiO-based LSCF catalyst were evaluated using H$_2$-TPR. H$_2$ consumption profiles of the catalysts were compared and shown in Fig. 3. The TPR profile of pure NiO showed two main reduction peaks centered at 390 and 500 °C, indicating reduction of Ni^{3+} ions to Ni^{2+} ions and reduction of Ni^{2+} ions to Ni^0 ions, respectively [46–50]. For LSCF, the lowest temperature of reduction at 270 °C was attributed to surface oxygen reduction [51], while bulk oxygen reduction took placed during higher temperatures at 505, 625, and 735 °C. The bulk oxygen reduction indicate three stages of reduction (1) reduction of Co^{3+}/Fe^{4+}, Fe^{5+}
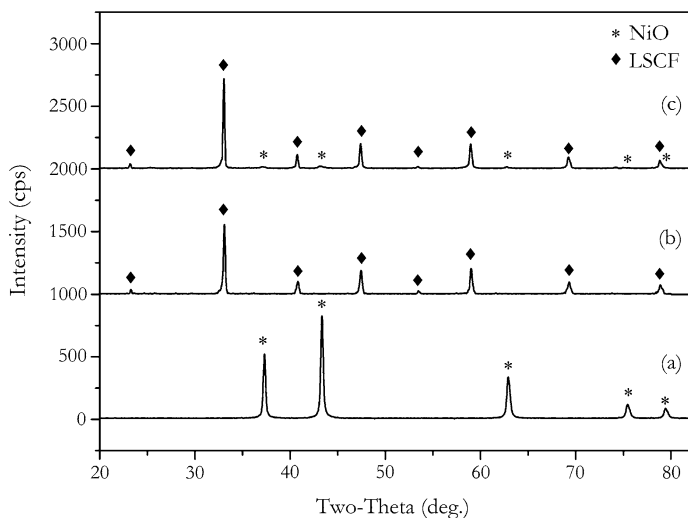
Fig. 2 The XRD patterns; (a) NiO, (b) LSCF, and (c) 10%NiO–LSCF
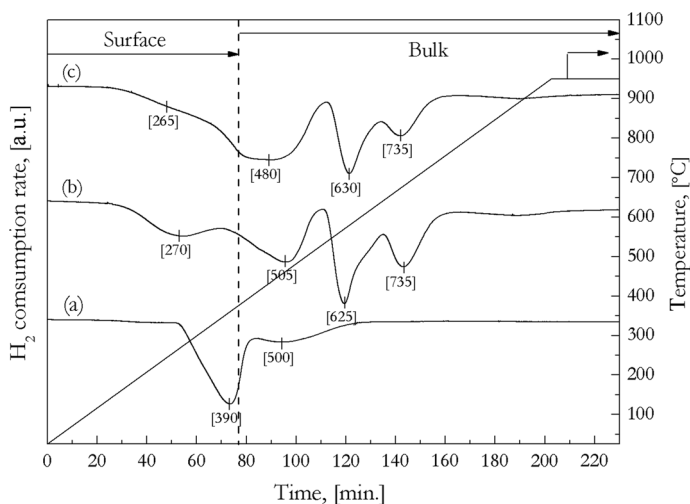
Fig. 3 H_2-TP–R profiles of synthesized catalysts; (a) NiO, (b) LSCF, and (c) 10%NiO–LSCF
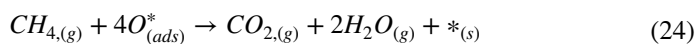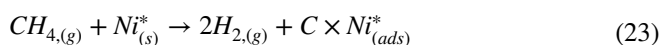
ions to Co^{2+}/Fe^{3+} ions at about 505 °C, (2) reduction of Co^{2+}/Fe^{3+} ions to Co^0/Fe^{2+} ions at 625 °C, and (3) reduction of Co^0/Fe^{2+} ions to Co^0/Fe^0 ions at 735 °C [51–53]. The reduction temperatures of 10%NiO–LSCF showed more similarity to that of LSCF rather than of NiO. This is because the NiO level was not high enough to dominate the crystal structure [46, 54–56]. The H_2 consumption could be interpreted as oxygen vacancy/oxygen lattice/oxygen storage capacity/oxygen deficiency, which was 11,188 μmol/g$_{solid}$, 5754 μmol/g$_{solid}$, and 6442 μmol/g$_{solid}$, for NiO, LSCF3773 and 10%NiO–LSCF3773, respectively. The 10%NiO was in situ reduced before each run at 500 °C, achieving Ni^0 ions which acts as an active site for the partial oxidation of methane.

## CH$_4$ Temperature-programmed surface reaction (CH$_4$-TPR)

CH$_4$ dissociation on the surface of 10%NiO-LSCF was characterized by CH$_4$-TPR technique, shown in Fig. 4. Four regions of temperature range can be considered according to its mechanisms.

No CH$_4$ consumption was detected at temperature lower than 450 °C, in this region I.

During temperature from 450 to 600 °C, referred to as region II in Fig. 4, CH$_4$ dissociation and combustion were presumably occurred on Ni active site (Eq. 23), and adsorbed oxygen on the surface $\left(O^*_{(ads)}\right)$ (Eq. 24) via Eley–Rideal mechanism,.

$$CH_{4,(g)} + Ni^*_{(s)} \rightarrow 2H_{2,(g)} + C \times Ni^*_{(ads)} \qquad (23)$$

$$CH_{4,(g)} + 4O^*_{(ads)} \rightarrow CO_{2,(g)} + 2H_2O_{(g)} + *_{(s)} \qquad (24)$$

A slight CH$_4$ consumption and rapid H$_2$ formation were correspondingly observed at the beginning of this region. Meanwhile, adsorbed oxygen on LSCF's
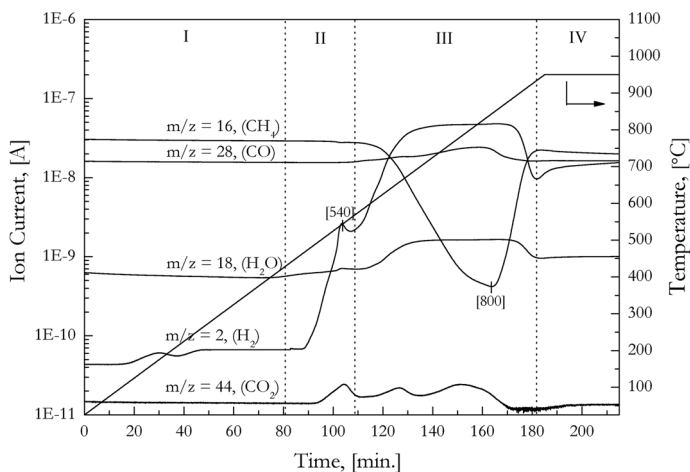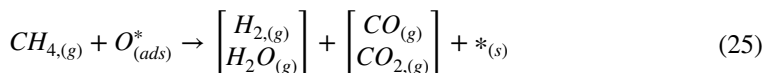
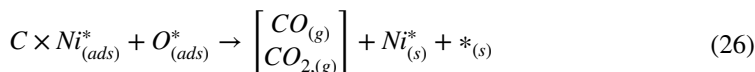**Fig. 4** CH_4-TPSR profiles of 10%NiO–LSCF catalyst

surface was reduced by CH_4, giving H_2O and CO_2 as gaseous products. During the process, the oxygen vacancies was achieved (Eq. 24). These oxygen vacancies are to be re-oxidized by gaseous N_2O during the N_2O decomposition.

During temperature from 600 to 900 °C, shown as region III in Fig. 4, CH4 was significantly consumed while all the gaseous products, H_2, CO, CO_2 and H_2O were found. Two main redox mechanisms were proposed as below:

(1) CH_4 partial oxidation/combustion occurred on the oxygen surface of LSCF, giving H_2, H_2O, CO, CO_2 and oxygen vacancies as products, shown below as Eq. 25.

$$CH_{4,(g)} + O_{(ads)}^* \rightarrow \begin{bmatrix} H_{2,(g)} \\ H_2O_{(g)} \end{bmatrix} + \begin{bmatrix} CO_{(g)} \\ CO_{2,(g)} \end{bmatrix} + *_{(s)} \tag{25}$$

(2) Langmuir–Hinshelwood surface reaction between the coked Ni site $\left((C \times Ni^*)_{(ads)} \right)$ (obtained from Eq. 23) and surface oxygen $\left(O_{(ads)}^* \right)$ was occurred, producing gaseous products of CO and CO_2. The oxygen vacancy $\left(*_{(s)} \right)$ was obtained as the result of coke combustion, between the adsorbed coke $\left((C \cdot Ni^*)_{(ads)} \right)$ and the lattice oxygen $\left(O_{(ads)}^* \right)$, represented by Eq. 26, where the coked-Ni site $\left((C \times Ni^*)_{(ads)} \right)$ was regenerated back to its original form of active Ni $\left(Ni_{(s)}^* \right)$. This regenerated Ni $\left(Ni_{(s)}^* \right)$ could react cyclically with CH_4 giving more H_2 and coked-Ni $\left((C \times Ni^*)_{(ads)} \right)$, according to Eq. 23. The coked-Ni $\left((C \times Ni^*)_{(ads)} \right)$ would consequently reduce the LSCF surface by reacting with lattice oxygen $\left(O_{(ads)}^* \right)$. The oxygen vacancy $\left(*_{(s)} \right)$ was then achieved via Eq. 26.

$$C \times Ni_{(ads)}^* + O_{(ads)}^* \rightarrow \begin{bmatrix} CO_{(g)} \\ CO_{2,(g)} \end{bmatrix} + Ni_{(s)}^* + *_{(s)} \tag{26}$$

(3) In the 4th region where the temperature was higher than 900 °C, CH_4 concentration returned back to its initial level due to the absence of the adsorbed oxygen on the surface of LSCF before started to slightly decrease again by CH_4 cracking over the coked-Ni active site. This resulted in an increase in H_2 formation, where the CO, CO_2 and H_2O concentration, more or less, remain unchanged. However, H_2O, CO, and CO_2 re-adsorption could be suggested.

$$CH_{4,(g)} + C \times Ni^*_{(ads)} \rightarrow 2C \times Ni^*_{(ads)} + 2H_{2,(g)} \tag{27}$$
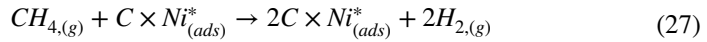
The results conclude that CH_4 combustion was dominant when the temperature was lower than 600 °C. The desired CH_4 partial oxidation occurred at temperature between 600 and 900 °C, while the CH_4 cracking took part at 900 °C and beyond.

Chemical equilibrium estimation and effect of operating temperature

Changes of the standard Gibbs free energy $\left(\Delta_r G^0\right)$ of the possible reactions listed in Table 1 were calculated using formulas in Table 2 shown below in Fig. 5. The selected temperature for the study was ranged from 500 to 1000 °C.

The result showed that the NO_2 formation (reaction 2) was theoretically not possible for all temperature range while CH_4 cracking could occur at temperature higher than 700 °C, approximately. From 500 to 600 °C, combustion of methane would be evidenced (reactions 4, 10, 11). Methane partial oxidation (reaction 4) would occur during temperature from 700 to 1000 °C. Coke formation could be deposited on the surface of the catalyst at temperature higher than 700 °C.

Figs. 6 and 7 present conversions of reactants and products of N_2O decomposition and CH_4 partial oxidation, which supposed to occurred at the feed side and permeate side of the membrane reactor, respectively.

Fig. 6a shows the highest N_2O conversion of 68.71 was in the non-catalytic reaction and complete N_2O conversion (99.13%) when using 10%NiO–LSCF as a
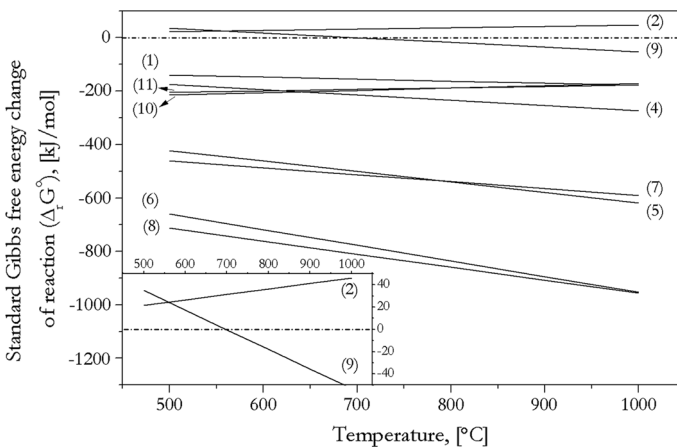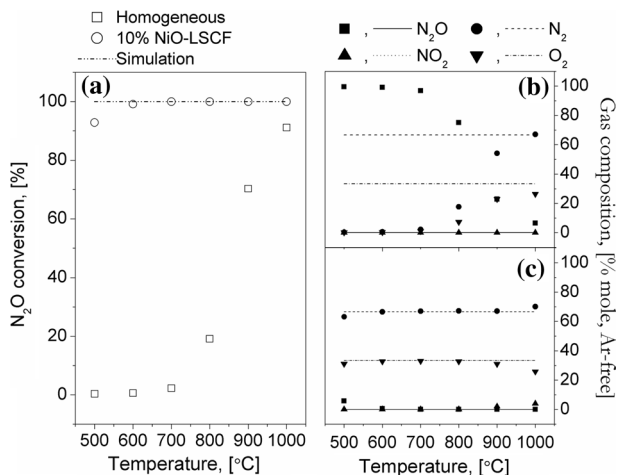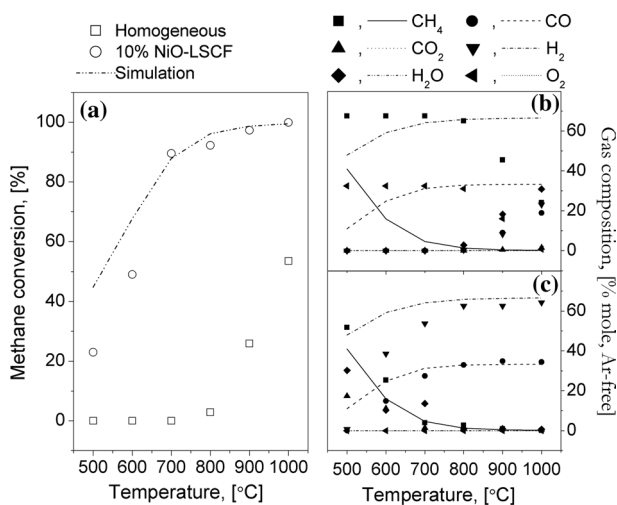

Fig. 5 Changes of the standard Gibbs free energy of each reactions

Fig. 6 **a** Conversion of the reactant (N_2O) as a function of temperature. Mole fraction product of N_2O decomposition using **b** no catalyst (homogeneous) and **c** 10%NiO–LSCF catalyst compared with equilibrium mole fraction using Aspen Plus program (line) run WHSV = 50 ml/g/min at 1 atm from 500 to 1000 °C

Fig. 7 **a** The temperature dependence of methane conversion. Mole fraction product at the permeate side of the membrane process using **b** no catalyst (homogeneous) and **c** 10%NiO–LSCF catalyst compared with equilibrium mole fraction using Aspen Plus program (line) run is WHSV = 50 ml/g min at 1 atm from 500 to 1000 °C
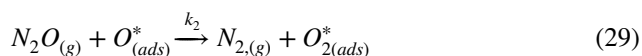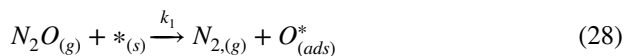
catalyst. The conversion was close to the theoretical when using the 10%NiO–LSCF catalyst.

Fig. 6b represents non-catalytic nitrous oxide decomposition. The highest N_2O conversion was obtained at 1000 °C giving N_2 and O_2 of 56.39 and 17.93 mol%, respectively, although both products began to be detectable at 800 °C. The

productivities were increased with increasing temperature. The ratio of N_2 to O_2 was around 2.3–2.4 to 1 which disagreed with theoretical ratio from stoichiometry (2 to 1). There was no NO_2 detected for all temperature range. In addition, NO was not measured in the experiment, although NO formation as an intermediate could be suggested via N_2O oxidation/decomposition.

Fig. 6c shows that complete N_2O conversion started to be achievable at 600 °C, giving 66.59 mol% of N_2 and 32.78mol% of O_2. Ratio of N_2 to O_2 was 2:1 during temperature from 600 to 800 °C, agreeing with its stoichiometry theoretically. At temperature higher than 800 C, the ratio was found to increase by the influence of oxygen inhibition, explained in the later part. The following reaction pathway could be suggested.

N_2O was adsorbed and dissociated on the oxygen vacancy, achieved by CH_4 partial oxidation via reaction (23)–(26), giving N_2 and surface oxygen $\left(O_{(ads)}^*\right)$, represented by Eq. 28. The resulting surface oxygen $\left(O_{(ads)}^*\right)$, was reacted further with gaseous N_2O via Eley–Rideal surface mechanism via Eq. (29), where more N_2 and adsorbed oxygen molecule $\left(O_{2\,(ads)}^*\right)$ were obtained. Afterwards, the adsorbed oxygen molecule $\left(O_{2\,(ads)}^*\right)$ could be; (i) desorbed giving gaseous O_2 while leaving the oxygen lattice vacant again $\left(*_{(s)}\right)$, demonstrated in Eq. 30, (ii) react with oxygen vacancy $\left(*_{(s)}\right)$ via Langmuir–Hinshelwood surface reaction, providing more surface oxygen $\left(O_{(ads)}^*\right)$, shown in Eq. 31.

$$N_2O_{(g)} + *_{(s)} \xrightarrow{k_1} N_{2,(g)} + O_{(ads)}^* \tag{28}$$

$$N_2O_{(g)} + O_{(ads)}^* \xrightarrow{k_2} N_{2,(g)} + O_{2(ads)}^* \tag{29}$$

$$O_{2(ads)}^* \xrightarrow{k_3} O_{2,(g)} + *_{(s)} \tag{30}$$

$$O_{2(ads)}^* + *_{(s)} \xrightarrow{k_4} 2O_{(ads)}^* \tag{31}$$

However, the gaseous oxygen produced via Eq. 30 could be re-adsorbed on the oxygen vacancy $\left(*_{(s)}\right)$, represented by Eq. 32. The surface oxygen was obtained.

$$O_{2,(g)} + 2*_{(s)} \xrightarrow{k_5} 2O_{(ads)}^* \tag{32}$$

Oxygen inhibition, where full surface coverage was achieved by oxygen re-adsorption, could occur if k_1, k_4 and/or k_5 is larger than k_2 and/or k_3. This would be evident by N_2 to O_2 ratio higher than 2. However, as the ratio of N_2 to O_2 was approximately 2 to, this implies that k_1, k_4 and/or k_5 is less than k_2 and/or k_3, meaning that reactions 28, 31 and/or 32 is the rate limiting step. At temperature from 900

to 1000 °C, the unwanted NO_2 formation was utilized the surface oxygen, allowing Eq. 32 to go more forward. This leads to the decrease of O_2, resulted in the higher ratio of N_2 to O_2. Mechanism of NO_2 formation was proposed below, where the N_2O adsorption/dissociation (reaction 28) occurred, then followed by the below Eley–Rideal surface reactions.
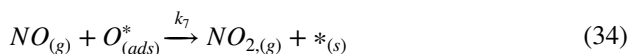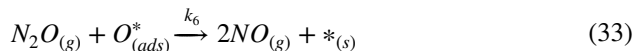
$$N_2O_{(g)} + O^*_{(ads)} \xrightarrow{k_6} 2NO_{(g)} + *_{(s)} \tag{33}$$

$$NO_{(g)} + O^*_{(ads)} \xrightarrow{k_7} NO_{2,(g)} + *_{(s)} \tag{34}$$

Fig. 6 (line) shows the equilibrium molar fraction of N_2 and O_2 at 0.67 and 0.33, calculated using Aspen Plus program, for all temperatures. NO_2 was not found. The results agreed with the calculation reported in Fig. 5, where reaction 1 was spontaneous and reaction 2 was thermodynamically limited. The catalytic conversion of N_2O and its productivities (Fig. 6c) were found to approach the equilibrium approximation as shown in (Fig. 6 (line)) especially during temperature from 500 to 900 °C.
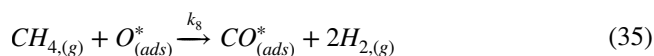
Fig. 7 shows CH_4 partial oxidation using no catalyst (b), in the presence of 10%NiO-LSCF (c), and (line) equilibrium concentration calculated using Aspen Plus program. From Fig. 7a, it can be seen that maximum CH_4 conversion in non-catalyst, achieved at 1000 °C, was 53.51. CH_4 consumption began to be observable at 800 °C, giving conversions of 2.87. In using 10%NiO–LSCF catalyst, complete conversion of CH_4 was obtained at 1000 °C, which gives conversion that are close to the theoretical.

From Fig. 7b, less than 3mol% fraction of H_2, CO_2, H_2O, C_2H_4, and C_2H_6 were produced at this temperature. Reverse water gas shift reaction (RWGS), which is the combination of reaction (10) and 11, was evident as H_2O production was noticed. The Boudouard reaction, the combination of reactions 4, 9, and 10, was not observed, as there was no CO_2 formation, therefore, coke formation did not occurred at this temperature range. On the other hand, CO_2 was detected at higher temperature ranging from 900 to 1000 °C, suggesting the possibility of the Boudouard reaction, therefore, coke formation was also predicted. In addition, H_2, CO, CO_2, and H_2O molar fraction were increased with increasing temperature. This indicated that complete combustion, reverse water gas shift and the Boudouard reaction were presumably taken place. However, C_2+ was increased at temperature from 800 to 900 °C, then decreased again at 900 to 1000 °C. This implied that reactions 5 and 7 were driven backward at temperature lower than 900 °C, and moved forward at temperature higher than 900 °C.

From Fig. 7c, H_2O and CO_2 were detected at temperature lower than 700 °C and found to decrease with increasing temperature. Small amount (less than 1mol%) of H_2O and CO_2 were found at temperature higher than 700 °C. On the other hand, H_2 and CO were increased with increasing temperature. The reaction temperatures of the CH_4 partial oxidation, CH_4 combustion and CH_4 cracking shown in Fig. 7c were correspondingly agreed with those shown in Fig. 4. The catalytic experimental result was found to approach the equilibrium composition,

shown in Fig. 7c, and corresponded with calculation of Gibbs free energy changes tabulated in Fig. 5. The negative value of ΔG^{o} of reaction 4 became larger with increasing temperature, while that of reactions 10 and 11 became smaller. This means that reaction 4 was more spontaneous at higher temperature leading to higher yield of H_2 and CO, while reaction 10 and 11 were more thermodynamically limited resulting in less amount of CO_2 and H_2O production. At temperature higher than 700 °C, the possible mechanism was proposed as follows;

The surface oxygen or lattice oxygen $\left(O_{(ads)}^* \right)$, produced from reaction (28), assumed to diffuse through the membrane from the feed side and reacted with CH_4, giving adsorbed CO $\left(CO_{(ads)}^* \right)$ and gaseous H_2 as shown in Eq. 35. The adsorbed CO $\left(CO_{(ads)}^* \right)$ was afterwards desorbed to gaseous CO and left the active site $\left({}^*_{(s)} \right)$ free again, represented by Eq. 36:

$$ CH_{4,(g)} + O_{(ads)}^* \xrightarrow{k_8} CO_{(ads)}^* + 2H_{2,(g)} \tag{35} $$

$$ CO_{(ads)}^* \xrightarrow{k_9} CO_{(g)} + {}^*_{(s)} \tag{36} $$

CO_2 and H_2O splitting were occurred on the oxygen vacancy $\left({}^*_{(s)} \right)$ as shown in Eq. (37) and (38), producing CO and H_2 as gaseous products. On the other hand, the oxygen vacancy $\left({}^*_{(s)} \right)$ was simultaneously re-oxidized by CO_2 and H_2O becoming the adsorbed oxygen $\left(O_{(ads)}^* \right)$;

$$ CO_{2,(g)} + {}^*_{(s)} \xrightarrow{k_{10}} CO_{(g)} + O_{(ads)}^* \tag{37} $$

$$ H_2O_{(g)} + {}^*_{(s)} \xrightarrow{k_{11}} H_{2,(g)} + O_{(ads)}^* \tag{38} $$
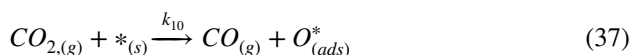
From Fig. 7c, no significant amount of C_2+ and C_3+ were found for all temperature range, indicating the occurrence of reaction (5), (6), (7), and (8) where C_2+ and C_3+ were reacted with oxygen giving H_2 and CO. The result agreed with the standard Gibbs free energy changes, calculated and shown in Fig. 5. From Fig. 5, the standard Gibbs free energy changes of reaction (9) was positive at temperature from 500 to 600 °C, and became negative at temperature higher than 600 °C. This means that coke formation via reaction (9) was not occurred at 500 to 600 °C, but instead was likely to occur at temperature higher than 600 °C.

Figure 8 compared syngas productivities and its ratio between obtained from catalytic process using 10%NiO–LSCF, and from the chemical equilibrium calculation. The experimental result was found to be in good agreement with the calculation. Syngas ratio was approaching 2 at temperature from 700 to 1000 °C.
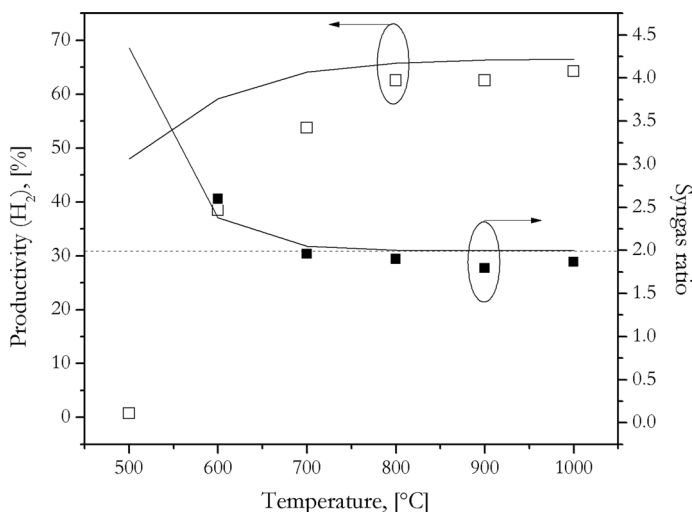
Fig. 8 Experimental catalytic performance using 10%NiO–LSCF compared with equilibrium composition

Conclusion

10%NiO–LSCF was a promising catalyst for high purity syngas production via methane partial oxidation using nitrous oxide as an oxidant in a membrane reactor. Surface mechanisms of the reactions, at both feed side and permeate side were proposed, based on the experimental results. The catalytic experimental result was in good agreement with the chemical equilibrium properties, calculated using Aspen Plus. The optimal operating temperature for the reaction carried out in a membrane reactor is 800 °C under atmosphere pressure. At this temperature, NO_2 formation was not occurred, and full conversion of N_2O decomposition at the feed side, and methane partial oxidation at the permeate side were achieved. Heavier hydrocarbons, i.e. C_2+ and C_3+, should not be found. High purity syngas could be obtained at the ratio of H_2 to CO equal to 2.

References

1. Li C, Shen Y, Zhu S, Shen S (2014) Supported Ni–La–Ox for catalytic decomposition of N_2O I: component optimization and synergy. RSC Adv 4(55):29107
2. Xue L, Zhang C, He H, Teraoka Y (2007) Catalytic decomposition of N_2O over CeO_2 promoted Co_3O_4 spinel catalyst. Appl Catal B 75(3–4):167–174
3. Liu Z, Zhou Z, He F, Chen B, Zhao Y, Xu Q (2017) Catalytic decomposition of N_2O over NiO–CeO_2 mixed oxide catalyst. Catal Today 293–294:56–60

4. Vitousek PM, Aber JD, Howarth RW, Likens GE, Matson PA, Schindler DW, Schlesinger WH, Tilmen DG (1997) Human alteration of the global nitrogen cycle: sources and consequences. Ecol Appl 7:737–750

5. van den Brink RW, Booneveld S, Verhaak MJFM, De Bruijn FA (2002) Selective catalytic reduction of N_2O and NO_x in a single reactor in the nitric acid industry. Catal Today 75:227–232

6. Ravishankara AR, Daniel JS, Portmann RW (2009) Nitrous oxide (N_2O): the dominant ozone-depleting substance emitted in the 21st century. Science 326(5949):123–125

7. Li L, Xu J, Hu J, Han J (2014) Reducing nitrous oxide emissions to mitigate climate change and protect the ozone layer. Environ Sci Technol 48(9):5290–5297

8. Pedros PB, Askari O, Metghalchi H (2016) Reduction of nitrous oxide emissions from biological nutrient removal processes by thermal decomposition. Water Res 106:304–311

9. Abu-Zied BM, Schwieger W, Unger A (2008) Nitrous oxide decomposition over transition metal exchanged ZSM-5 zeolites prepared by the solid-state ion-exchange method. Appl Catal B 84(1–2):277–288

10. Rivallan M, Ricchiardi G, Bordiga S, Zecchina A (2009) Adsorption and reactivity of nitrogen oxides (NO_2, NO, N_2O) on Fe-zeolites. J Catal 264(2):104–116

11. Khan NA, Kennedy EM, Dlugogorski BZ, Adesina AA, Stockenhuber M (2014) Partial oxidation of methane with nitrous oxide forms synthesis gas over cobalt exchanged ZSM-5. Catal Commun 53:42–46

12. Ruiz-Trejo E, Boldrin P, Medley-Hallam JL, Darr J, Atkinson A, Brandon NP (2015) Partial oxidation of methane using silver/gadolinia-doped ceria composite membranes. Chem Eng Sci 127:269–275

13. Indarto A (2016) Partial oxidation of methane to methanol with nitrogen dioxide in dielectric barrier discharge plasma: experimental and molecular modeling. Plasma Sources Sci Technol 25(2):025002

14. Lee S-J, Ryu I-S, Kim B-M, Moon S-H (2011) A review of the current application of N_2O emission reduction in CDM projects. Int J Greenhouse Gas Control 5(1):167–176

15. Zeng HC, Pang XY (1997) Catalytic decomposition of nitrous oxide on alumina-supported ruthenium catalysts Ru/Al_2O_3. Appl Catal B 13:113–122

16. Slagterna Å, Swaan HM, Olsbyea U, Dahla IM, Mirodatosb C (1998) Catalytic partial oxidation of methane over Ni-, Co- and Fe-Based catalysts. Catal Today 46:107–115

17. Yuzaki K, Yarimizu T, Aoyagi K, Ito S, Kunimori K (1998) Catalytic decomposition of N_2O over supported Rh catalysts: effects of supports and Rh dispersion. Catal Today 45:129–134

18. Marnasidou KG, Voutetakis SS, Tjatjopoulos GJ, Vasalos IA (1999) Catalytic partial oxidation of methane to synthesis gas in a pilot-plant-scale spouted-bed reactor. Chem Eng Sci 54:3691–3699

19. Ohno Y, Kimura K, Bi M, Matsushima T (1999) The translational energy of desorbing products in NO and N_2O decomposition on Pd (110). J Chem Phys 110(17):8221–8224

20. Huang C, Zhu Y, Wang X, Liu X, Wang J, Zhang T (2017) Sn promoted $BaFeO_{3-\delta}$ catalysts for N_2O decomposition: optimization of Fe active centers. J Catal 347:9–20

21. Li K, Wang XF, Zeng HC (1997) Kinetics of N_2O Decomposition on a RuO_2/Al_2O_3 Catalyst. Chem Eng Res Des 75(8):807–812

22. Zhu J, Vanommen J, Lefferts L (2006) Effect of surface OH groups on catalytic performance of yttrium-stabilized ZrO_2 in partial oxidation of CH_4 to syngas. Catal Today 117(1–3):163–167

23. Fleys M, Shan W, Simon Y, Marquaire P (2007) Detailed kinetic study of the partial oxidation of methane over La_2O_3 catalyst. Part 1: experimental results. Ind Eng Chem Res 46:1063–1068

24. Fleys M, Simon Y, Marquaire P (2007) Detailed kinetic study of the partial oxidation of methane over La_2O_3 catalyst. Part 2: mechanism. Ind Eng Chem Res 46:1069–1078

25. Dacquin JP, Lancelot C, Dujardin C, Da Costa P, Djega-Mariadassou G, Beaunier P, Kaliaguine S, Vaudreuil S, Royer S, Granger P (2009) Influence of preparation methods of $LaCoO_3$ on the catalytic performances in the decomposition of N_2O. Appl Catal B 91(3–4):596–604

26. Wu Y, Cordier C, Berrier E, Nuns N, Dujardin C, Granger P (2013) Surface reconstructions of $LaCo_{1-x}Fe_xO_3$ at high temperature during N_2O decomposition in realistic exhaust gas composition: impact on the catalytic properties. Appl Catal B 140–141:151–163

27. Ivanov DV, Pinaeva LG, Sadovskaya EM, Isupova LA (2016) Isotopic transient kinetic study of N_2O decomposition on $LaMnO_{3+\delta}$. J Mol Catal A 412:34–38

28. Yang Z, Zhang Y, Ding W (2014) Investigation on the reforming reactions of coke-oven-gas to H_2 and CO in oxygen-permeable membrane reactor. J Membr Sci 470:197–204

29. Cheng H, Lu X, Hu D, Zhang Y, Ding W, Zhao H (2011) Hydrogen production by catalytic partial oxidation of coke oven gas in $BaCo_{0.7}Fe_{0.2}Nb_{0.1}O_{3-\delta}$ membranes with surface modification. Int J Hydrogen Energy 36(1):528–538

30. Zhu X, Li Q, He Y, Cong Y, Yang W (2010) Oxygen permeation and partial oxidation of methane in dual-phase membrane reactors. J Membr Sci 360(1–2):454–460

31. Song S, Zhang P, Han M, Singhal SC (2012) Oxygen permeation and partial oxidation of methane reaction in $Ba_{0.9}Co_{0.7}Fe_{0.2}Nb_{0.1}O_{3-\delta}$ oxygen permeation membrane. J Membr Sci 415–416:654–662

32. Jin W, Li S, Huang P, Xu N, Shi J, Lin YS (2000) Tubular lanthanum cobaltite perovskite-type membrane reactors for partial oxidation of methane to syngas. J Membr Sci 166:13–22

33. Li S, Jin W, Huang P, Xu N, Shi J, Lin YS (2000) Tubular lanthanum cobaltite perovskite type membrane for oxygen permeation. J Membr Sci 166:51–61

34. Figen HE, Baykara SZ (2018) Effect of ruthenium addition on molybdenum catalysts for syngas production via catalytic partial oxidation of methane in a monolithic reactor. Int J Hydrogen Energy 43(2):1129–1138

35. Swamy CS, Christopher J (1992) Decomposition of N_2O on perovskite-related oxides. Catal Rev 34(4):409–425

36. Babiniec SM, Coker EN, Miller JE, Ambrosini A (2015) Investigation of $La_xSr_{1-x}Co_yM_{1-y}O_{3-\delta}$ (M = Mn, Fe) perovskite materials as thermochemical energy storage media. Sol Energy 118:451–459

37. Koh A, Chen L, Keeleong W, Johnson B, Khimyak T, Lin J (2007) Hydrogen or synthesis gas production via the partial oxidation of methane over supported nickel-cobalt catalysts. Int J Hydrogen Energy 32(6):725–730

38. Kangsadan T, Srisurat T, Kim P, Laosiripojana N, Jindasuwan S, Hartley UW (2015) Hydrogen production from palmitic acid through autothermal reforming: thermodynamic analysis. Eng J 19(4):153–165

39. Zhang J, Haribal V, Li F (2017) Perovskite nanocomposites as effective CO_2-splitting agents in a cyclic redox scheme. Sci Adv 3(8):e1701184

40. Kapteijn F, RodriguezMirasol J, Moulijn JA (1996) Heterogeneous catalytic decomposition of nitrous oxide. Appl Catal B 9:25–64

41. Smith JM, Van Ness HC, Abbott MM (2005) Introduction to chemical engineering thermodynamics, 7th edn. McGraw Hill, New York

42. Felder RM, Rousseau RW (2005) Elementary principles of chemical processes, 3rd edn. Wiley, New York

43. Yaws CL (1996) Handbook of thermodynamics diagram. Gulf Publishing Company, Houston

44. Standard thermodynamic properties of chemical substances.

45. Speight JG (2017) Rules of thumb for petroleum engineers, 1st edn. Wiley, Hoboken

46. Pavlova S, Kapokova L, Bunina R, Alikina G, Sazonova N, Krieger T, Ishchenko A, Rogov V, Gulyaev R, Sadykovab V, Mirodatosc C (2012) Syngas production by CO_2 reforming of methane using $LnFeNi(Ru)O_3$ perovskites as precursors of robust catalysts. Catal Sci Technol 2:2099–2108

47. Xu X, Li L, Yu F, Peng H, Fang X, Wang X (2017) Mesoporous high surface area NiO synthesized with soft templates: remarkable for catalytic CH_4 deep oxidation. Mol Catal 441:81–91

48. Bai G, Dai H, Deng J, Liu Y, Qiu W, Zhao Z, Li X, Yang H (2013) The microemulsion preparation and high catalytic performance of mesoporous NiO nanorods and nanocubes for toluene combustion. Chem Eng J 219:200–208

49. Araujo GCd, Lima SMd, Assaf JM, Peña MA, Fierro JLG, do Carmo Rangel M (2008) Catalytic evaluation of perovskite-type oxide $LaNi_{1-x}Ru_xO_3$ in methane dry reforming. Catal Today 133–135:129–135

50. Shan W (2003) Reduction property and catalytic activity of $Ce_{1-x}Ni_xO_2$ mixed oxide catalysts for CH_4 oxidation. Appl Catal A General 246(1):1–9

51. Cihlar J, Vrba R, Castkova K, Cihlar J (2017) Effect of transition metal on stability and activity of La-Ca-M-(Al)-O (M = Co, Cr, Fe and Mn) perovskite oxides during partial oxidation of methane. Int J Hydrogen Energy 42(31):19920–19934

52. Zhao K, Zheng A, Li H, He F, Huang Z, Wei G, Shen Y, Zhao Z (2017) Exploration of the mechanism of chemical looping steam methane reforming using double perovskite-type oxides $La_{1.6}Sr_{0.4}FeCoO_6$. Appl Catal B 219:672–682

53. Li R, Yu C, Shen S (2002) Partial oxidation of methane to syngas using lattice oxygen of $La_{1-x}Sr_xFeO_3$ perovskite oxide catalysts instead of molecular oxygen. J Nat Gas Chem 117:137–144

54. Singha RK, Shukla A, Yadav A, Sivakumar Konathala LN, Bal R (2017) Effect of metal-support interaction on activity and stability of Ni-CeO$_2$ catalyst for partial oxidation of methane. Appl Catal B 202:473–488
55. Zheng Y, Li K, Wang H, Tian D, Wang Y, Zhu X, Wei Y, Zheng M, Luo Y (2017) Designed oxygen carriers from macroporous LaFeO$_3$ supported CeO$_2$ for chemical-looping reforming of methane. Appl Catal B 202:51–63
56. Pal P, Singha RK, Saha A, Bal R, Panda AB (2015) Defect-induced efficient partial oxidation of methane over nonstoichiometric Ni/CeO$_2$ nanocrystals. J Phys Chem C 119(24):13610–13618